Letter

Switchable skyrmion–antiskyrmion tubes in rhombohedral $BaTiO_3$ and related materials

Fernando Gómez-Ortiz,[*,†] Louis Bastogne,[*] Sriram Anand, Miao Yu, Xu He, and Philippe Ghosez[‡]
Theoretical Materials Physics, Q-MAT, Université de Liège, B-4000 Sart-Tilman, Belgium

(Received 21 December 2024; accepted 12 May 2025; published 27 May 2025)

Skyrmions are stable topological textures that have garnered substantial attention within the ferroelectric community for their exotic functional properties. While previous studies have questioned the feasibility of $[001]_{pc}$ skyrmion tubes in rhombohedral $BaTiO_3$ due to the high-energy cost of 180°domain walls, we demonstrate here their stabilization with topological charges of $\mathcal{Q} = \pm 1$ from density functional theory and second-principles calculations. By enabling extensive vortex and antivortex polarization configurations, the expected prohibitive energetic barriers are overcome while preserving the topological nature of the structures. Notably, we extend these findings to demonstrate the appearance of skyrmion and antiskyrmion tubes in other related materials, highlighting their broader relevance. Furthermore, our computational experiments indicate that these structures can be directly stabilized and reversibly switched by applied electric fields, establishing a straightforward route for their practical realization and functional control in nanoelectronic devices.

DOI: 10.1103/PhysRevB.111.L180104

Skyrmions have garnered significant interest in condensed matter physics due to their unique topological properties, which impart remarkable stability against perturbations [1]. First observed as two-dimensional magnetic textures [2], skyrmions can extend into three dimensions as cylindrical or tubular structures called skyrmion tubes, which maintain translational invariance along a specific axis [3].

Analogous nanoscale polarization textures have been predicted [4–6] and observed [7] in ferroelectric materials (although it was suggested they might not be ubiquitous [8]), drawing attention due to their smaller size [5] and fascinating functional properties including negative capacitance [9,10], emergent chirality [11–13], or ultrafast dynamics [14–16].

Despite experimental efforts, ferroelectric skyrmion tubes have so far only been experimentally observed in superlattices, while their emergence in bulk materials remains elusive. Among potential candidates, $PbTiO_3$ was theoretically proposed [5] owing to its capacity to host noncollinear polar arrangements within its domain walls [17], yet experimental confirmation of their topological nature remains unachieved.

In contrast, recent findings predicted fractional skyrme lines in rhombohedral $BaTiO_3$ confined within 180° domain walls [18]. However, the authors were unable to stabilize ordinary skyrmions. Interestingly, antiskyrmion tubes with $\mathcal{Q} = -2$ have been predicted in $BaTiO_3$ when the columnar nanodomain aligns with the polarization easy axis in any $\langle 111 \rangle_{pc}$ direction, broadening the scope of topological structures in this material [6]. Besides, meron-antimeron lattices have also been stabilized by means of acoustic phonon excitations [19]. Adding to this promising landscape, recent experiments have shown vortex-antivortex lattices in twisted $BaTiO_3$ freestanding layers [20] and center-convergent polar domains in $BaTiO_3$ nanoislands [21]. Amazingly, despite ferroelectricity in $BaTiO_3$ being first reported almost 80 years ago [22], new discoveries continue to emerge recurrently. These findings position $BaTiO_3$ as a promising candidate for skyrmion observation in bulk ferroelectrics.

In this Letter, combining density functional theory (DFT) and second-principles [23,24] calculations, we report the stabilization of translationally invariant polarization textures along the $[001]_{pc}$ direction in $BaTiO_3$ characterized by skyrmion numbers of $\mathcal{Q} = \pm 1$. Computational experiments demonstrate the stabilization and controllable switching of these textures, offering a clear route to their practical realization. Notably, this is a demonstration of skyrmions and antiskyrmions in the same ferroelectric system under identical conditions. Additionally, we generalize our findings to other related materials such as $KNbO_3$. Our results challenge recent interpretations [6,18], which rejected the existence of these type of skyrmion tubes in rhombohedral ferroelectrics due to the prohibitive energy cost of the resultant 180° domain walls. Here, we show that if the polarization in the matrix is allowed to form a vortex- or antivortexlike texture, the energetic constraints are alleviated, enabling their stabilization.

Results: $[001]_{pc}$*-oriented skyrmion tubes*. In light of the computational experiment presented in Ref. [5] where a columnar nanodomain was embedded in a matrix of antiparallel polarization within tetragonal $PbTiO_3$, it is natural to wonder whether similar nanocolumns can be stabilized in rhombohedral ferroelectrics such as $BaTiO_3$ or $KNbO_3$. Building on this concept, we construct a $[001]_{pc}$-oriented nanocolumn in rhombohedral $BaTiO_3$ where the Ti displacements responsible for the in-plane and out-of-plane polarization components are intentionally adjusted to achieve the desired configuration. The DFT equilibrium structure obtained after relaxation (see details in the Supplemental

[*]These authors contributed equally to this work.
[†]Contact author: fgomez@uliege.be
[‡]Contact author: philippe.ghosez@uliege.be

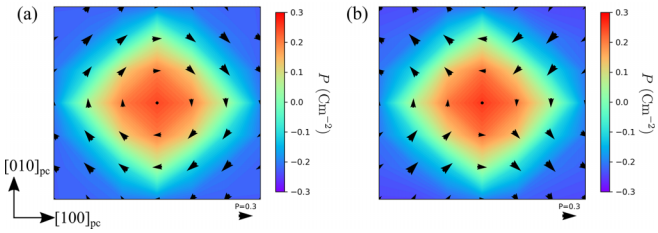

FIG. 1. (a) DFT equilibrium skyrmion texture obtained after relaxation of manually imposed initial Ti displacements. (b) Equilibrium antiskyrmion texture obtained after relaxation of the skyrmion texture after reverting the sign of the displacements along x. Arrows indicate the in-plane components of the polarization, whereas the color map represents the out-of-plane polarization computed as explained in the Supplemental Material [25], and the supercell size used is $7\times7\times1$.

Material [25] and references therein [26–38]) is presented in Fig. 1(a).

Notably, in $PbTiO_3$ skyrmions [5], the $[111]_{pc}$-oriented antiskyrmion tube in $BaTiO_3$ [6], and the skyrme lines appearing in 180° domains in $BaTiO_3$ [18], the noncollinear character of the polarization is confined within the domain wall. In contrast, our results demonstrate that the Bloch character of the domain extends throughout the matrix of antiparallel polarization after relaxation. As shown in Fig. 1(a), even though the out-of-plane polar nanocolumn is confined to few unit cells, the vortexlike disturbance of the field, reflected by the in-plane components of the polarization, extends throughout the whole supercell. This behavior can be attributed to two main factors: (i) The development of an in-plane polarization component reduces elastic energy, allowing each cell to locally adopt a configuration closer to the nearest $\langle111\rangle_{pc}$ $R3m$ ground state, and (ii) it mitigates the formation of energetically unfavorable 180° domains, which would otherwise be prohibitively costly, as reported in Refs. [6,18].

Interestingly, a similar behavior is reported in Ref. [5], where $PbTiO_3$ skyrmion tubes exhibit a comparable response when subject to an expansive tensile strain exceeding a critical threshold. This observation suggests that such behavior could, in fact, be more general and extendable to other rhombohedral ferroelectrics. Notably, we demonstrate here that similar structures can also be stabilized in $KNbO_3$ (see Figs. S1 and S2 [25]), further reinforcing this idea.

Importantly, even though the continuous deformation from a homogeneous background to a vortexlike polarization configuration in the matrix helps stabilize the structure, it does not alter its topological properties. The nontrivial topology of a skyrmion tube can be computed by integrating the Pontryagin density (see Supplemental Material [25] and references therein [39]). As shown in Fig. S3(a) [25], an integer value of $\mathcal{Q}=1$ is obtained for the polar texture schematized in Fig. 1(a), proving its nontrivial character.

Unlike the antiskyrmions observed in Ref. [6], the skyrmions reported here exhibit a chiral nature. The existence of chiral behavior can be experimentally probed using resonant soft x-ray diffraction-based circular dichroism measurements (RSXD-CD) [11,12,40–42], and is a property of significant relevance for light-matter interactions, with potential applications in optoelectronics [43].

Computationally, the chirality can be computed by means of the helicity [12,44–46]. As shown in Fig. S3(c) [25], the chiral nature of the skyrmion tube is determined by the coupling between the in-plane polarization rotation and the polarization value at the core, granting a nonzero net value.

Due to the periodic boundary conditions and the Poincaré-Hopf theorem [47], the total vorticity in the simulation supercell must sum to zero. Consequently, the vortex and antivortex textures must counterbalance each other. As it can be observed in Fig. 1(a), the antivortex is located at the middle of the cell edges. One may wonder whether the center of the nanocolumn could be positioned at the antivortex core to stabilize an antiskyrmion with a topological charge of $\mathcal{Q}=-1$ in place of a skyrmion. This can be accomplished by reversing the sign of the atomic displacements along the x direction of the skyrmion texture with respect to the cubic reference, effectively transforming vortices into antivortices and vice versa.

Interestingly, and in contrast to tetragonal $PbTiO_3$ [5], we find that the position of the nanocolumn is flexible and decoupled from the in-plane components, allowing it to align with the antivortex core and stabilizing an antiskyrmion, as illustrated in Fig. 1(b). The DFT energy of the structure is almost degenerate with that of the skyrmion (within the accuracy of DFT, see Fig. S2 [25]), demonstrating that rhombohedral ferroelectrics can host both skyrmion and antiskyrmion textures under identical strain and growing conditions.

Finally, we go a step further by revealing the existence of two distinct types of skyrmions and antiskyrmions: one centered at Ti sites and the other at Ba sites. Although initially stabilized by intentional Ti displacements, resulting in vortex and antivortex cores centered at the Ti sites, we found that configurations with the vortex/antivortex singularity centered at the Ba sites are also stable. Notably, the Ba-centered configurations are energetically more favorable, lying 1.2 meV/f.u. lower than their Ti-centered counterparts in our $7\times7\times1$ supercell. This is explained from the fact that the vortex or antivortex cores represent the intersection of the two domain walls between the up/down and right/left in-plane polarization components which are more stable when centered on the Ba site [48]. We report a detailed energy analysis of both types of skyrmion/antiskyrmion pairs together with nudged elastic band (NEB) [35–37] calculations to compute the energy barriers between them in Fig. S4 [25].

Orientation, size effects, and stability of skyrmion tubes. The energy and stability of skyrmion tubes are analyzed across different nanocolumn orientations and radii as well as various supercell sizes. Given the comparable energetics of the Ba/Ti-centered skyrmion and antiskyrmion textures, we focus our analysis on the Ti-centered skyrmion case for simplicity. Orientation effects are examined with DFT, while stability and size effects are studied with second-principles methods (details in Supplemental Material [25]).

Energetics with increasing nanocolumn size. The impact of nanocolumn size on the defect's energy is explored for a fixed supercell length, $L=21$ u.c. Interestingly, stable nanocolumns as small as $r=1$ u.c. are found as shown in Fig. 2(a). This value is smaller than those encountered for in

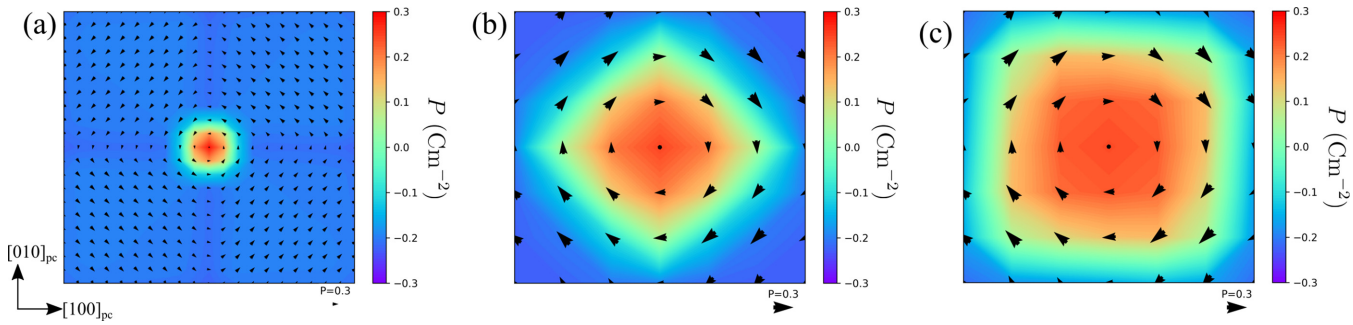

FIG. 2. Stabilization of different defects in $BaTiO_3$. (a) $r = 1$ u.c. nanocolumn stabilized with the second-principles model. (b) Rhombus and (c) squarelike oriented cross sections of the nanocolumn. Arrows indicate the in-plane components of the polarization, whereas the color map represents the out-of-plane polarization computed as explained in the Supplemental Material [25], where the supercell sizes used are $21\times21\times1$ and $7\times7\times1$.

Ref. [6], where textures with radii smaller than 4 u.c. decay to a monodomain configuration [6]. The defect energy scales linearly with the square root of the nanocolumn area, and metastable states exist at different sizes. For instance, doubling the radius to $r = 2$ u.c. raises the energy by $\Delta E = 0.07$ meV/f.u., highlighting the tunability of nanocolumn size.

Influence of the orientation of the nanocolumn's cross section. As the skyrmion tube is oriented along the [001] direction, its cross sections exhibit a cubic shape. This contrasts with the hexagonal-like cross sections reported in Ref. [6]. Square nanocolumns align either rhombically [domain walls along $\{110\}_{pc}$, Fig. 2(b)] or cubically [domain walls along $\{100\}_{pc}$, see Fig. 2(c)]. Both configurations are stable with an energy difference of 0.1 meV/f.u. in our $7\times7\times1$ supercell. However, attributing this energy difference solely to the domain orientation is challenging, as a change in orientation inevitably results in a change in the area of the nanocolumn which also influences (in a similar magnitude) the total energy as we have just discussed. What we can conclude anyway, is that the energy landscape associated with varying the orientation of the nanocolumn's cross section is extremely flat, allowing for multiple realizations and potential dynamical transitions between them at finite temperatures as we show in the Supplemental Video 1 [25].

Energetics with increasing supercell size. Keeping a fixed value of two unit cells for the nanocolumn, we can increase the value of the supercell in which the defect is embedded, i.e., $L = 7,\ 11,\ 13,\ 15,\ 17,\ 19,\ 21$. As already discussed above, although the nanocolumn size is fixed, the in-plane polarization components extend across the supercell, locally resembling the $\langle111\rangle_{pc}$ $R3m$ configuration, leading to an asymptotic energy behavior as shown in Fig. S5 [25]. This allows us to quantify the energy difference between the defect and the rhombohedral monodomain phase in the infinite supercell limit. As the supercell grows, regions resembling the $\langle111\rangle_{pc}$ monodomain expand uniformly, while the defect's energy contribution remains constant. A power-law model, $E = E_d + a/(x + b)$, accurately describes this behavior (see residuals in Fig. S5 [25]).

The asymptotic energy obtained with respect to the cubic reference is $E_d = -24.87 \pm 0.01$ meV/f.u., closely matching that of the rhombohedral monodomain phase ($E_{R3m} = -24.94$ meV/f.u.) and lying below the orthorhombic monodomain phase ($E_{Amm2} = -22.29$ meV/f.u.). This result indicates that the defect introduces only a minor, localized energy disturbance, despite inducing a large-scale disruption in the polarization pattern, highlighting the narrow energy window within which these phases coexist.

Stability of the skyrmion tubes. Finally, we investigate the stability of skyrmion and antiskyrmions under thermal fluctuations, finding them equally robust. However, Ti-centered defects remain stable up to a critical temperature of $T = 150$ K, whereas Ba-centered defects are stable up to $T = 80$ K. Beyond these thresholds, the nanocolumns collapse into a monodomain out-of-plane polarization, while the in-plane vortex components persist. Despite their lower energy, Ba-centered defects exhibit a lower barrier to transitioning into the homogeneous state, as quantified by NEB calculations (Fig. S6 [25]). The transition path is detailed in Supplemental Videos 2 and 3 [25].

Stabilization and switching via applied electric fields. So far, we have focused on the metastability of skyrmions and antiskyrmions in rhombohedral $BaTiO_3$, where these structures are constructed by intentionally imposing atomic displacements and subsequently relaxing the configurations. In this section, we demonstrate how these textures can be stabilized using inhomogeneous electric fields, also providing an experimental pathway for their realization.

In order to stabilize the in-plane components of the polarization we rely on spatially modulated electric fields. In Fig. 3(a) we schematically show an initial polarization texture. Experimentally, this could be achieved by sequentially activating contiguous electrodes in a stepwise manner, as depicted in the schematic. Numerically, we impose an electric field of 1 MV/cm modulated along x and directed along y by a cosine function in order to comply with periodic boundary conditions and study the evolution of the system ($L = 17$ u.c.) with finite-temperature simulations at $T = 10$ K. In tetragonal ferroelectrics, such electric fields will result in the stabilization of 180° domain walls with the polarization aligned along y. However, due to the rhombohedral nature of $BaTiO_3$, in-plane polarization components along the x direction will also develop as well as out-of-plane components resulting in a more complex structure [see Fig. 3(d)]. The direction of the in-plane polarization components along the x axis can vary and show an erratic behavior, as shown in Fig. 3(d), varying depending on the specific realization. However, applying now an electric field oriented along x and modulating along the y direction

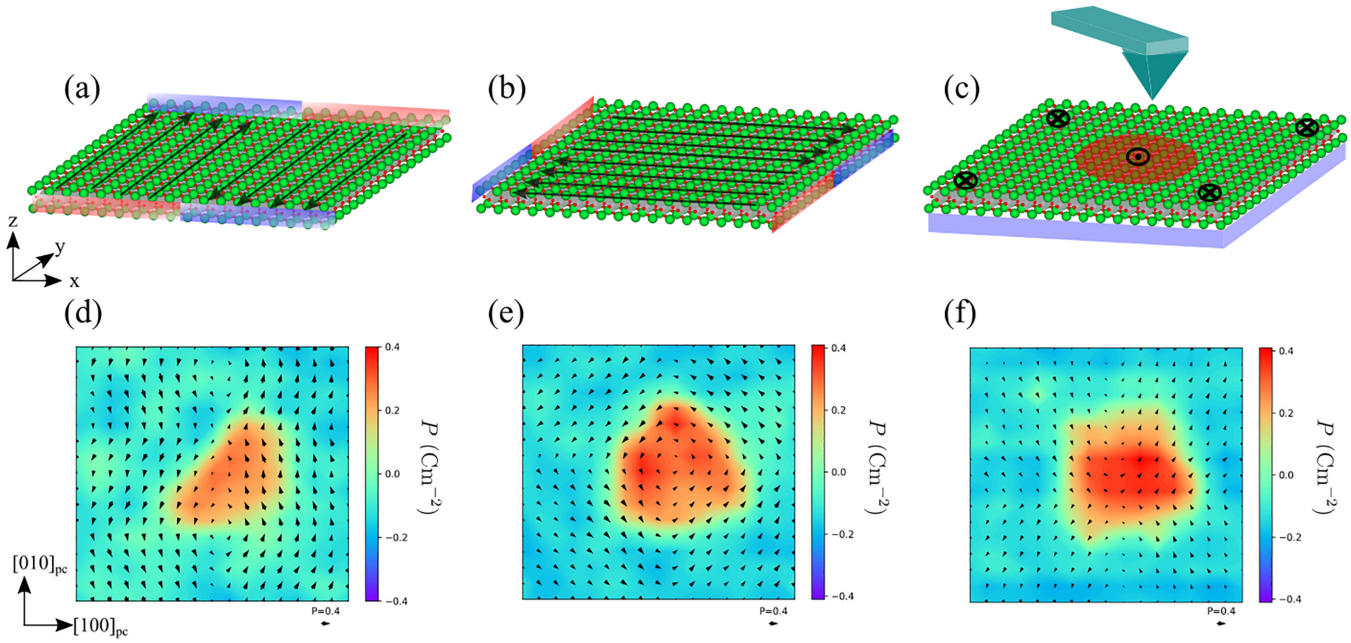

FIG. 3. Schematic view of the computational experiment. (a)–(c) The black arrows denote the desired polarization direction within the material. The red and blue stripes represent electrodes, which can be sequentially activated in a stepwise manner during experimental implementations to achieve the intended polarization. (a) Polarization field modulated along the x direction and directed along y. (b) Polarization field modulated along y and directed along x. (c) Control of the out-of-plane components achievable by with an AFM tip. (d) Obtained structure after the application of a modulated electric field as described in the main text. (e) Skyrmion texture after in-plane and out-of-plane components have been controlled with the application of extra fields in configurations (b) and (c). (f) Antiskyrmion texture obtained from (e) after reverting the polarity of the electric field shown in (b). Arrows indicate the in-plane components of the polarization, whereas the color map represents the out-of-plane polarization computed as explained in the Supplemental Material [25]. The supercell size is $17\times17\times1$.

allows effective control over these in-plane components. This second field induces polarizations along the x axis, similar to those illustrated in Fig. 3(b). Utilizing such a configuration will stabilize a vortex, while reversing the polarity of this second field will result in the stabilization of an antivortex texture, as shown in Figs. 3(e) and 3(f), respectively. Furthermore, this procedure can be applied recursively; by alternating the polarity of the second electric field, we can achieve a controlled switching between vortex and antivortex states, as demonstrated in Supplemental Video 4 [25]. Alternatively, activating simultaneously the electrodes shown in Fig. 3(a) will already stabilize an antivortex texture as shown in the Supplemental Material [25] due to the electric fields generated between contiguous electrodes. Importantly, due to the nature of the domain walls only a Ba-centered vortex/antivortex can be stabilized in this way.

Similar to the in-plane components, the out-of-plane components will vary depending on the realization when no bias is applied to the sample. To achieve a localized nanocolumn, as shown in Figs. 3(e) and 3(f), a Gaussian field as achievable with an atomic force microscopy (AFM) tip has been applied on top of a homogeneous background of opposite polarization [Fig. 3(c)]. Experimentally, a homogeneous out-of-plane polarization could first be established via scanning, followed by local reversal to achieve the desired nanocolumn. An important aspect to highlight is that once the nanocolumn is established, it remains stable, and the switching of the in-plane components does not affect it, in agreement with the DFT results that proved the flexibility of the out-of-plane components to adjust to vortex and antivortex cores. This stability enables the transition from a skyrmion to antiskyrmion to occur without the need for an electric field applied along the z direction. Because the in-plane polarization components extend over a large scale, as discussed throughout this Letter, highly spatially modulated electric fields are not required, facilitating the experimental implementation of this setup.

Discussion. In this Letter, we have successfully demonstrated, from density functional theory and second-principles calculations, the stabilization of two different types (Ba- and Ti-centered) of translationally invariant polarization textures along the $[001]_{pc}$ direction in rhombohedral $BaTiO_3$, characterized by skyrmion numbers of $\mathcal{Q} = \pm1$. This constitutes a theoretical prediction where ferroelectric skyrmions and antiskyrmions are stable in the same material under identical conditions. Our results provide strong evidence that such structures can also be generalized to other rhombohedral ferroelectrics, such as $KNbO_3$ which keeps a rhombohedral phase close to room temperature, broadening the scope of materials capable of hosting complex polar textures and potentially enabling their stabilization under practical operating conditions.

Importantly, our findings challenge the prevailing understanding that $\mathcal{Q} = \pm1$ skyrmion tubes are energetically unfeasible in rhombohedral ferroelectrics with fixed antiparallel polarization values, where the energy cost of 180° domain walls has been considered prohibitive [6,18]. By allowing the polarization matrix to adopt a vortex- or antivortexlike configuration, we demonstrated that these energy constraints

can be alleviated while preserving the topological character of the system. Furthermore, this extended nature of the Bloch component to the entire matrix can potentially facilitate its experimental observation [8].

Additionally, we have delved into various orientations and sizes for the nanocolumn. In contrast to $[111]_{pc}$ $BaTiO_3$ antiskyrmion tubes [6], cubic cross sections are found for our skyrmion tubes where rhombus or square orientations are possible for the nanocolumn being essentially degenerate in energy. The diameter of the nanocolumn is found to be of about 1 nm, even smaller than the ones reported for $\mathcal{Q} = -2$ antiskyrmions [6]. The energy of the defect in the large-scale limit is found to be surprisingly close to the rhombohedral ground state, indicating that the defect introduces only a minor and localized energy disturbance.

Finally, we have demonstrated how these textures can be stabilized and reversibly switched using spatially modulated electric fields, proposing an experimental setup for their realization. Moreover, due to the chiral nature of the skyrmionic state, it can also be experimentally probed by RSXD-CD techniques. This represents a system in which the topological charge of a skyrmion can be controlled from $\mathcal{Q} = +1$ to $\mathcal{Q} = -1$ using external electric fields.

This work not only expands the current phase diagram of $BaTiO_3$ but also underscores the potential for stabilizing skyrmion-based polar textures in other ferroelectrics, offering different avenues for the design of materials with tunable topological properties.

Acknowledgments. The authors acknowledge useful discussions with Céline Lichtensteiger. F.G.-O., L.B., and Ph.G. acknowledge support by the European Union's Horizon 2020 research and innovation program under Grant Agreement No. 964931 (TSAR). F.G.-O. also acknowledges financial support from MSCA-PF 101148906 funded by the European Union and the Fonds de la Recherche Scientifique (FNRS) through the Grant No. FNRS-CR 1.B.227.25F. Ph.G. and X.H. also acknowledge support from the Fonds de la Recherche Scientifique (FNRS) through the PDR projects PROMOSPAN (Grant No. T.0107.20) and TOPOTEX (Grant No. T.0128.25). S.A. acknowledges financial support from the EIT Raw Materials–AMIS Joint Master Program.

Data availability. All data are available in the main text or the Supplemental Material [25]. The second-principles model is open source and available at Ref. [49] along with a validation assessment.

[1] N. Nagaosa and Y. Tokura, Topological properties and dynamics of magnetic skyrmions, Nat. Nanotechnol. **8**, 899 (2013).

[2] S. Mühlbauer, B. Binz, F. Jonietz, C. Pfleiderer, A. Rosch, A. Neubauer, R. Georgii, and P. Böni, Skyrmion lattice in a chiral magnet, Science **323**, 915 (2009).

[3] D. Wolf, S. Schneider, U. K. Rößler, A. Kovács, M. Schmidt, R. E. Dunin-Borkowski, B. Büchner, B. Rellinghaus, and A. Lubk, Unveiling the three-dimensional magnetic texture of skyrmion tubes, Nat. Nanotechnol. **17**, 250 (2022).

[4] Y. Nahas, S. Prokhorenko, L. Louis, Z. Gui, I. Kornev, and L. Bellaiche, Discovery of stable skyrmionic state in ferroelectric nanocomposites, Nat. Commun. **6**, 8542 (2015).

[5] M. A. P. Gonçalves, C. Escorihuela-Sayalero, P. García-Fernández, J. Junquera, and J. Íñiguez, Theoretical guidelines to create and tune electric skyrmion bubbles, Sci. Adv. **5**, eaau7023 (2019).

[6] M. A. P. Gonçalves, M. Paściak, and J. Hlinka, Antiskyrmions in ferroelectric barium titanate, Phys. Rev. Lett. **133**, 066802 (2024).

[7] S. Das, Y. L. Tang, Z. Hong, M. A. P. Gonçalves, M. R. McCarter, C. Klewe, K. X. Nguyen, F. Gómez-Ortiz, P. Shafer, E. Arenholz, V. A. Stoica, S.-L. Hsu, B. Wang, C. Ophus, J. F. Liu, C. T. Nelson, S. Saremi, B. Prasad, A. B. Mei, D. G. Schlom *et al.*, Observation of room-temperature polar skyrmions, Nature (London) **568**, 368 (2019).

[8] E. Zatterin, P. Ondrejkovic, L. Bastogne, C. Lichtensteiger, L. Tovaglieri, D. A. Chaney, A. Sasani, T. Schülli, A. Bosak, S. Leake, P. Zubko, P. Ghosez, J. Hlinka, J.-M. Triscone, and M. Hadjimichael, Assessing the ubiquity of Bloch domain walls in ferroelectric lead titanate superlattices, Phys. Rev. X **14**, 041052 (2024).

[9] J. Íñiguez, P. Zubko, I. Luk'yanchuk, and A. Cano, Ferroelectric negative capacitance, Nat. Rev. Mater. **4**, 243 (2019).

[10] S. Das, Z. Hong, V. A. Stoica, M. A. P. Gonçalves, Y. T. Shao, E. Parsonnet, E. J. Marksz, S. Saremi, M. R. McCarter, A. Reynoso, C. J. Long, A. M. Hagerstrom, D. Meyers, V. Ravi, B. Prasad, H. Zhou, Z. Zhang, H. Wen, F. Gómez-Ortiz, P. García-Fernández *et al.*, Local negative permittivity and topological phase transition in polar skyrmions, Nat. Mater. **20**, 194 (2021).

[11] L. Louis, I. Kornev, G. Geneste, B. Dkhil, and L. Bellaiche, Novel complex phenomena in ferroelectric nanocomposites, J. Phys.: Condens. Matter **24**, 402201 (2012).

[12] P. Shafer, P. García-Fernández, P. Aguado-Puente, A. R. Damodaran, A. K. Yadav, C. T. Nelson, S.-L. Hsu, J. C. Wojdeł, J. Íñiguez, L. W. Martin, E. Arenholz, J. Junquera, and R. Ramesh, Emergent chirality in the electric polarization texture of titanate superlattices, Proc. Natl. Acad. Sci. USA **115**, 915 (2018).

[13] K. T. Kim, M. R. McCarter, V. A. Stoica, S. Das, C. Klewe, E. P. Donoway, D. M. Burn, P. Shafer, F. Rodolakis, M. A. P. Gonçalves, F. Gómez-Ortiz, J. Íñiguez, P. García-Fernández, J. Junquera, S. Susarla, S. W. Lovesey, G. van der Laan, S. Y. Park, L. W. Martin, J. W. Freeland *et al.*, Chiral structures of electric polarization vectors quantified by x-ray resonant scattering, Nat. Commun. **13**, 1769 (2022).

[14] R. Zhu, Z. Jiang, X. Zhang, X. Zhong, C. Tan, M. Liu, Y. Sun, X. Li, R. Qi, K. Qu, Z. Liu, M. Wu, M. Li, B. Huang, Z. Xu, J. Wang, K. Liu, P. Gao, J. Wang, J. Li *et al.*, Dynamics of polar skyrmion bubbles under electric fields, Phys. Rev. Lett. **129**, 107601 (2022).

[15] H. Aramberri and J. Íñiguez-González, Brownian electric bubble quasiparticles, Phys. Rev. Lett. **132**, 136801 (2024).

[16] S. Prokhorenko, Y. Nahas, V. Govinden, Q. Zhang, N. Valanoor, and L. Bellaiche, Motion and teleportation of polar bubbles in low-dimensional ferroelectrics, Nat. Commun. **15**, 412 (2024).

[17] J. C. Wojdeł and J. Íñiguez, Ferroelectric transitions at ferroelectric domain walls found from first principles, Phys. Rev. Lett. **112**, 247603 (2014).

[18] C. Halcrow and E. Babaev, Fractional skyrme lines in ferroelectric barium titanate, Phys. Rev. Res. **6**, L032011 (2024).

[19] L. Bastogne, F. Gómez-Ortiz, S. Anand, and P. Ghosez, Dynamical manipulation of polar topologies from acoustic phonon excitations, Nano Lett. **24**, 13783 (2024).

[20] G. Sánchez-Santolino, V. Rouco, S. Puebla, H. Aramberri, V. Zamora, M. Cabero, F. A. Cuellar, C. Munuera, F. Mompean, M. Garcia-Hernandez, A. Castellanos-Gomez, J. Íñiguez, C. Leon, and J. Santamaria, A 2D ferroelectric vortex pattern in twisted $BaTiO_3$ freestanding layers, Nature (London) **626**, 529 (2024).

[21] I. Olaniyan, I. Tikhonov, V. V. Hevelke, S. Wiesner, L. Zhang, A. Razumnaya, N. Cherkashin, S. Schamm-Chardon, I. Lukyanchuk, D.-J. Kim, and C. Dubourdieu, Switchable topological polar states in epitaxial $BaTiO_3$ nanoislands on silicon, Nat. Commun. **15**, 10047 (2024).

[22] W. J. Merz, The electric and optical behavior of $BaTiO_3$ single-domain crystals, Phys. Rev. **76**, 1221 (1949).

[23] J. C. Wojdeł, P. Hermet, M. P. Ljungberg, P. Ghosez, and J. Íñiguez, First-principles model potentials for lattice-dynamical studies: General methodology and example of application to ferroic perovskite oxides, J. Phys.: Condens. Matter **25**, 305401 (2013).

[24] C. Escorihuela-Sayalero, J. C. Wojdeł, and J. Íñiguez, Efficient systematic scheme to construct second-principles lattice dynamical models, Phys. Rev. B **95**, 094115 (2017).

[25] See Supplemental Material at http://link.aps.org/supplemental/10.1103/PhysRevB.111.L180104 for computational details, a comparison between *A*- and *B*-centered defects in $BaTiO_3$ and $KNbO_3$, and an in-depth analysis of the corresponding energy landscape.

[26] M. J. Van Setten, M. Giantomassi, E. Bousquet, M. J. Verstraete, D. R. Hamann, X. Gonze, and G.-M. Rignanese, The PseudoDojo: Training and grading a 85 element optimized norm-conserving pseudopotential table, Comput. Phys. Commun. **226**, 39 (2018).

[27] X. Gonze, B. Amadon, G. Antonius, F. Arnardi, L. Baguet, J.-M. Beuken, J. Bieder, F. Bottin, J. Bouchet, E. Bousquet *et al.*, The ABINIT project: Impact, environment and recent developments, Comput. Phys. Commun. **248**, 107042 (2020).

[28] X. Gonze and C. Lee, Dynamical matrices, born effective charges, dielectric permittivity tensors, and interatomic force constants from density-functional perturbation theory, Phys. Rev. B **55**, 10355 (1997).

[29] D. R. Hamann, Optimized norm-conserving Vanderbilt pseudopotentials, Phys. Rev. B **88**, 085117 (2013).

[30] S. Duane, A. D. Kennedy, B. J. Pendleton, and D. Roweth, Hybrid Monte Carlo, Phys. Lett. B **195**, 216 (1987).

[31] J. Zhang, L. Bastogne, X. He, G. Tang, Y. Zhang, P. Ghosez, and J. Wang, Structural phase transitions and dielectric properties of $BaTiO_3$ from a second-principles method, Phys. Rev. B **108**, 134117 (2023).

[32] R. Fletcher, *Practical Methods of Optimization* (Wiley, Hoboken, NJ, 2000).

[33] M. Betancourt, A conceptual introduction to Hamiltonian Monte Carlo, arXiv:1701.02434.

[34] B. Meyer and D. Vanderbilt, *Ab initio* study of ferroelectric domain walls in $PbTiO_3$, Phys. Rev. B **65**, 104111 (2002).

[35] D. Sheppard, R. Terrell, and G. Henkelman, Optimization methods for finding minimum energy paths, J. Chem. Phys. **128**, 134106 (2008).

[36] G. Henkelman and H. Jónsson, Improved tangent estimate in the nudged elastic band method for finding minimum energy paths and saddle points, J. Chem. Phys. **113**, 9978 (2000).

[37] H. Jonsson, G. Mills, and K. W. Jacobsen, Nudged elastic band method for finding minimum energy paths of transitions, in *Classical and Quantum Dynamics in Condensed Phase Simulations*, edited by B. J. Berne, G. Ciccotti, and D. F. Coker (World Scientific, Singapore, 1998), pp. 385–404.

[38] L. Wan, T. Nishimatsu, and S. Beckman, The structural, dielectric, elastic, and piezoelectric properties of $KNbO_3$ from first-principles methods, J. Appl. Phys. **111**, 104107 (2012).

[39] B. Berg and M. Lüscher, Definition and statistical distributions of a topological number in the lattice O(3) σ-model, Nucl. Phys. B **190**, 412 (1981).

[40] S. W. Lovesey and G. van der Laan, Resonant x-ray diffraction from chiral electric-polarization structures, Phys. Rev. B **98**, 155410 (2018).

[41] J.-Y. Chauleau, T. Chirac, S. Fusil, V. Garcia, W. Akhtar, J. Tranchida, P. Thibaudeau, I. Gross, C. Blouzon, A. Finco, M. Bibes, B. Dkhil, D. D. Khalyavin, P. Manuel, V. Jacques, N. Jaouen, and M. Viret, Electric and antiferromagnetic chiral textures at multiferroic domain walls, Nat. Mater. **19**, 386 (2020).

[42] M. R. McCarter, K. T. Kim, V. A. Stoica, S. Das, C. Klewe, E. P. Donoway, D. M. Burn, P. Shafer, F. Rodolakis, M. A. P. Gonçalves, F. Gómez-Ortiz, J. Íñiguez, P. García-Fernández, J. Junquera, S. W. Lovesey, G. van der Laan, S. Y. Park, J. W. Freeland, L. W. Martin, D. R. Lee *et al.*, Structural chirality of polar skyrmions probed by resonant elastic x-ray scattering, Phys. Rev. Lett. **129**, 247601 (2022).

[43] Y. Shen, Q. Zhang, P. Shi, L. Du, X. Yuan, and A. V. Zayats, Optical skyrmions and other topological quasiparticles of light, Nat. Photon. **18**, 15 (2024).

[44] J. Junquera, Y. Nahas, S. Prokhorenko, L. Bellaiche, J. Íñiguez, D. G. Schlom, L.-Q. Chen, S. Salahuddin, D. A. Muller, L. W. Martin, and R. Ramesh, Topological phases in polar oxide nanostructures, Rev. Mod. Phys. **95**, 025001 (2023).

[45] H. Moffatt and R. Ricca, Helicity and the Călugăreanu invariant, Proc. R. Soc. London, Ser. A **439**, 411 (1992).

[46] H. K. Moffatt, Helicity and singular structures in fluid dynamics, Proc. Natl. Acad. Sci. USA **111**, 3663 (2014).

[47] J. Milnor, *Topology from the Differentiable Viewpoint* (The University Press of Virginia, Charlottesville, 1965).

[48] J. Padilla, W. Zhong, and D. Vanderbilt, First-principles investigation of 180° domain walls in $BaTiO_3$, Phys. Rev. B **53**, R5969 (1996).

[49] The second-principles model used in the calculations is available at https://doi.org/10.58119/ULG/M8BCYC, along with a validity passport.